LETTER

doi:10.1038/nature14648

The role of ridges in the formation and longevity of flat slabs

Sanja Knezevic Antonijevic[1], Lara S. Wagner[2], Abhash Kumar[1], Susan L. Beck[3], Maureen D. Long[4], George Zandt[3], Hernando Tavera[5] & Cristobal Condori[5]

Flat-slab subduction occurs when the descending plate becomes horizontal at some depth before resuming its descent into the mantle. It is often proposed as a mechanism for the uplifting of deep crustal rocks ('thick-skinned' deformation) far from plate boundaries, and for causing unusual patterns of volcanism, as far back as the Proterozoic eon[1]. For example, the formation of the expansive Rocky Mountains and the subsequent voluminous volcanism across much of the western USA has been attributed to a broad region of flat-slab subduction beneath North America that occurred during the Laramide orogeny (80–55 million years ago)[2]. Here we study the largest modern flat slab, located in Peru, to better understand the processes controlling the formation and extent of flat slabs. We present new data that indicate that the subducting Nazca Ridge is necessary for the development and continued support of the horizontal plate at a depth of about 90 kilometres. By combining constraints from Rayleigh wave phase velocities with improved earthquake locations, we find that the flat slab is shallowest along the ridge, while to the northwest of the ridge, the slab is sagging, tearing, and re-initiating normal subduction. On the basis of our observations, we propose a conceptual model for the temporal evolution of the Peruvian flat slab in which the flat slab forms because of the combined effects of trench retreat along the Peruvian plate boundary, suction, and ridge subduction. We find that while the ridge is necessary but not sufficient for the formation of the flat slab, its removal is sufficient for the flat slab to fail. This provides new constraints on our understanding of the processes controlling the beginning and end of the Laramide orogeny and other putative episodes of flat-slab subduction.

Oceanic plates subduct at different angles ranging from steep to shallow, with flat slabs representing the horizontal endmember. The subduction of buoyant aseismic ridges and plateaus comprising overthickened oceanic crust has long been thought to play a part in the formation of flat slabs[3]. More recent work has identified other potential contributing factors, including trench retreat[4,5], rapid overriding plate motion[4,5], and suction between the flat slab and overriding continental mantle lithosphere[5]. Many of these studies do not preclude the need for additional buoyancy from overthickened oceanic crust. However, a few recent studies suggest that subducting ridges do not affect the formation or sustainability of flat slabs[6,7].

To evaluate the influence of subducting ridges on the evolution of flat slabs, we focus on the flat slab in southern Peru (Fig. 1). Here, the subducting Nazca Ridge trends at an oblique angle to relative plate motion, resulting in a northward migration of the overriding continent relative to the down-going ridge[8]. We have collected and analysed data from two deployments of broadband seismometers in central and southern Peru: PULSE (Peru Lithosphere and Slab Experiment)[9], and CAUGHT (Central Andean Uplift and Geodynamics of High Topography)[10]. We also incorporate data from eight stations from the PERUSE deployment (Peru Slab Experiment)[11] and the permanent station called NNA in Lima, Peru (Fig. 1). Here we present a three-dimensional model of shear-wave velocity structure between −10° and −18°, obtained from the inversion of earthquake-generated Rayleigh-wave-phase velocities (Fig. 2 and Extended Data Figs 2–10). We also relocate slab seismicity across our study area using a double difference methodology (Figs 2 and 3, Extended Data Fig. 1 and Supplementary Table 1) (see Methods for details).

Our tomographic images and improved earthquake locations show the flat slab to be shallowest along the present-day projected location of the subducted Nazca Ridge (Figs 2g and 3g, h). To the south (Fig. 2h), the slab transitions abruptly from flat to normal, and earthquake locations align with an increase in shear-wave velocity in our model. To the north, where previous studies have proposed a broad flat slab of relatively uniform depth[12,13], we see a gradual but marked deepening of the plane of seismicity associated with subducted slab known as the Wadati–Benioff zone (Figs 2e, f and 3g, h). To the east, high shear-wave velocities associated with the flat slab extend substantially inboard (that is, away from the trench, inland) than the seismically active portion of the plate (Figs 2g and 3g,h). The downward bend

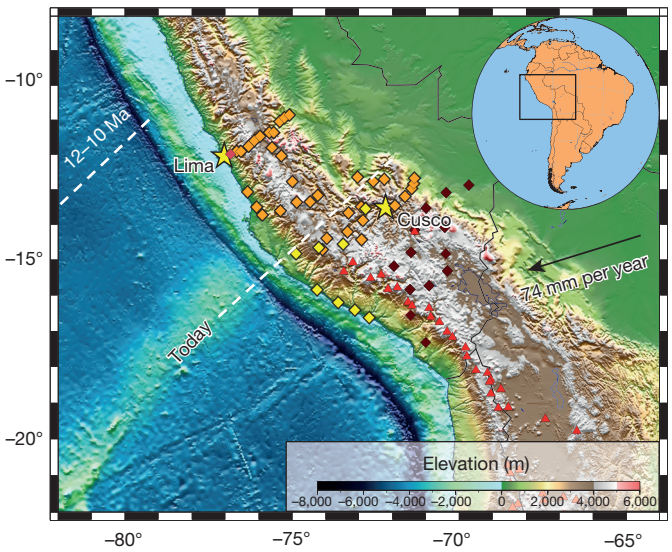

Figure 1 | Reference map of the Peruvian flat-slab region, illustrating the subducting Nazca Ridge beneath the advancing South American plate. Diamonds represent seismic stations used in this study: orange, PULSE; dark red, CAUGHT; yellow, PERUSE; red, the permanent NNA station. Yellow stars represent the cities Lima and Cusco. Red triangles represent volcanoes active during the Holocene epoch. The black arrow indicates the relative motion of the South American plate with respect to the Nazca Plate[21]. Dotted white lines show the estimated position of the Nazca Ridge 12–10 Ma and today[8].

[1]Department of Geological Sciences, University of North Carolina at Chapel Hill, CB 3315, Chapel Hill, North Carolina 27599, USA. [2]Department of Terrestrial Magnetism, Carnegie Institution for Science, 5241 Broad Branch Road NW, Washington DC 20015, USA. [3]Department of Geosciences, University of Arizona, 1040 East 4th Street, Tucson, Arizona 85721, USA. [4]Department of Geology and Geophysics, Yale University, 210 Whitney Avenue, New Haven, Connecticut 06511, USA. [5]Instituto Geofísico del Perú, Calle Badajoz 169, Lima 15012, Peru.

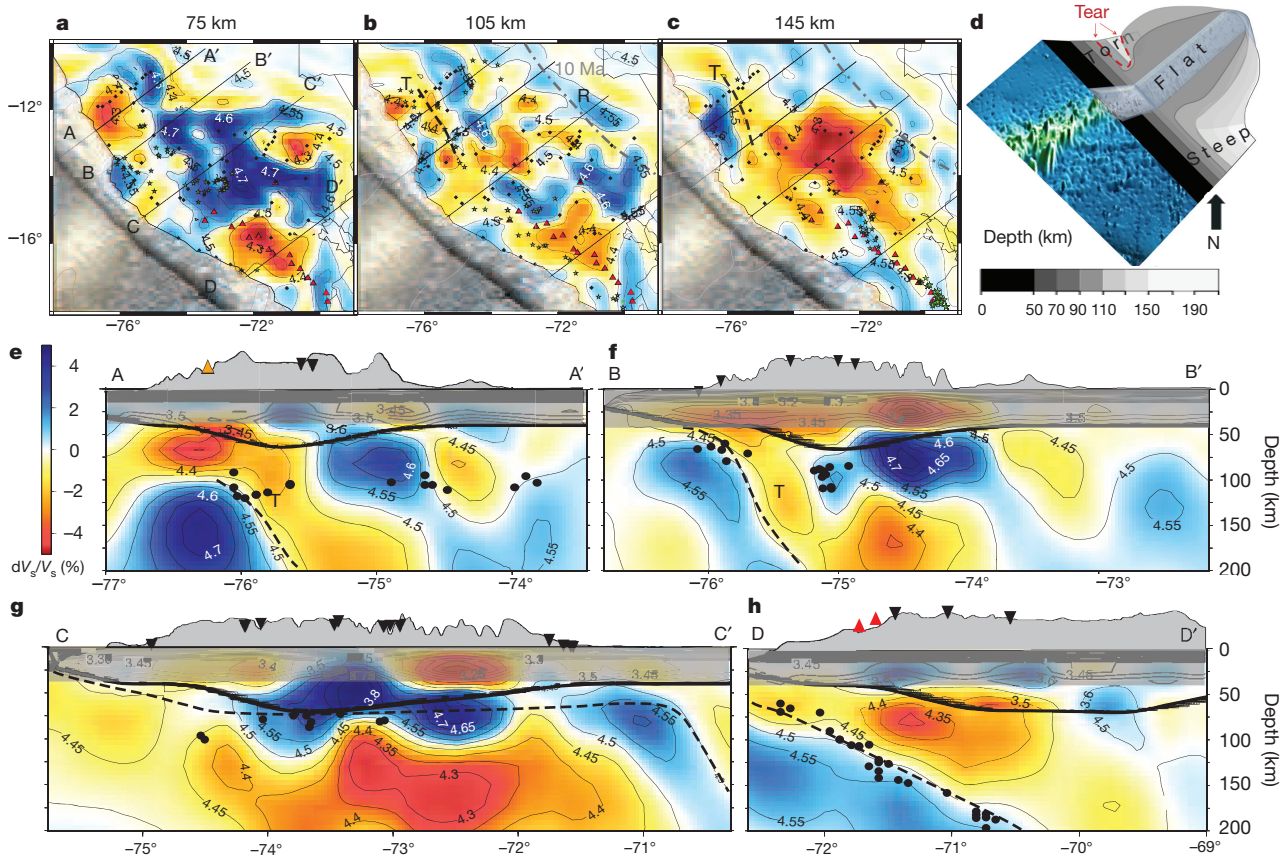

Figure 2 | Three-dimensional model of the structure of shear-wave velocities between −10° and −18°. **a**–**c**, Shear-wave velocities and seismicity at depths of 75 km (**a**), 105 km (**b**) and 145 km (**c**), and transects along the northern reinitiating steep slab (A–A′, B–B′), flat slab (C–C′) and southern steep slab (D–D′) segments. Colours indicate velocity deviations, dV_s/V_s (%); contours show absolute velocities in kilometres per second (numbered). **a**–**c**, Black circles represent stations used in our study; red triangles are Holocene volcanoes; green stars are earthquakes within 20 km of the depth shown; black lines refer to cross-sections shown in **e**–**h**. The grey dashed line in **b** and **c** shows the location of the trench 10 Ma (ref. 8); the black dashed line (labelled 'T') indicates the location of the slab tear. 'R' refers to the resumption of steep subduction at the eastern edge of the flat slab. **d**, Inferred flat-slab geometry along the Nazca Ridge track, and slab tear north of the ridge. **e**–**h**, Cross-sections of slab segments shown in **a**–**c**. Black dots show earthquake locations from this study; black inverted triangles are stations; red triangles are Holocene volcanoes; orange triangle represents the location of a measurement of unusually high heat flow[15]. Dashed lines show the inferred top of the slab. The thick black line shows the crustal thickness.

in the high-velocity plate at the easternmost extent of the flat slab appears to coincide with the location of the Peruvian trench about 10 million years ago (Ma)[8].

Of particular note is the geometry of the subducted plate north of the projected Nazca Ridge track (Fig. 2a–c, e, f). Here, we observe a dipping high-velocity anomaly to the trenchward side of a dipping low-velocity anomaly. We note the similarity between these structures (in an area previously believed to comprise typical flat slab) and those observed to the south beneath the active arc (Fig. 2e, f, h). We also note the difference between these structures and those adjacent to the ridge, where the continuous flat slab is well resolved (Fig. 2e–g and Extended Data Figs 3, 6–10). We interpret the westward-dipping low-velocity region parallel to the trench to be evidence of asthenosphere (the viscous, weak region of the upper mantle) between two torn portions of subducted plate. The dipping high-velocity anomaly to the west indicates the presence of a normally dipping slab extending to a depth of at least 200 km. This is consistent with the location of shear-wave scatterers identified from converted phases in earlier studies[14]. We propose that the subhorizontal seismicity to the east of the tear is located in remnant flat slab that has not yet been fully subducted. Local shear wave splitting studies show that shear waves move faster parallel to the trench[9], consistent with north–south-directed asthenospheric flow through a break in the Nazca plate. We also note the presence of a localized high heat flow (196 mW s^{-2}) above this low-velocity anomaly[15] (Fig. 2e). Along the northernmost transect, the location of the slab is not well resolved above a depth of about 100 km (Fig. 2e). Future work using ambient noise tomography may help us to resolve the slab geometry here, by providing improved constraints on velocities at shallower depths.

We incorporate the results of previous geodynamic modelling studies with our results, to create a conceptual model of the temporal evolution of the Peruvian flat slab (Fig. 3). We begin with the initiation of ridge subduction at approximately 11.2 Ma (ref. 8), before which we assume normal subduction across our study area (Fig. 3a). From there, we base our proposed temporal evolution of the Peruvian flat slab on four principles.

First, we present our conceptual model from the reference frame of a laterally stationary Nazca plate. Second, while most of the Nazca plate sinks vertically at a relatively constant rate, the plate containing the Nazca Ridge ceases to sink at a depth of about 90 km (Fig. 3b–f). We propose that this is due to buoyancy imparted by the overthickened oceanic crust and harzburgite layer associated with the ridge, consistent with previous modelling studies[16]. Third, we observe that the modern inboard extent of the Peruvian flat slab corresponds to the location of the trench at about 10 Ma. Given that the projected location of the Nazca Ridge extends further to the east, this finding suggests that

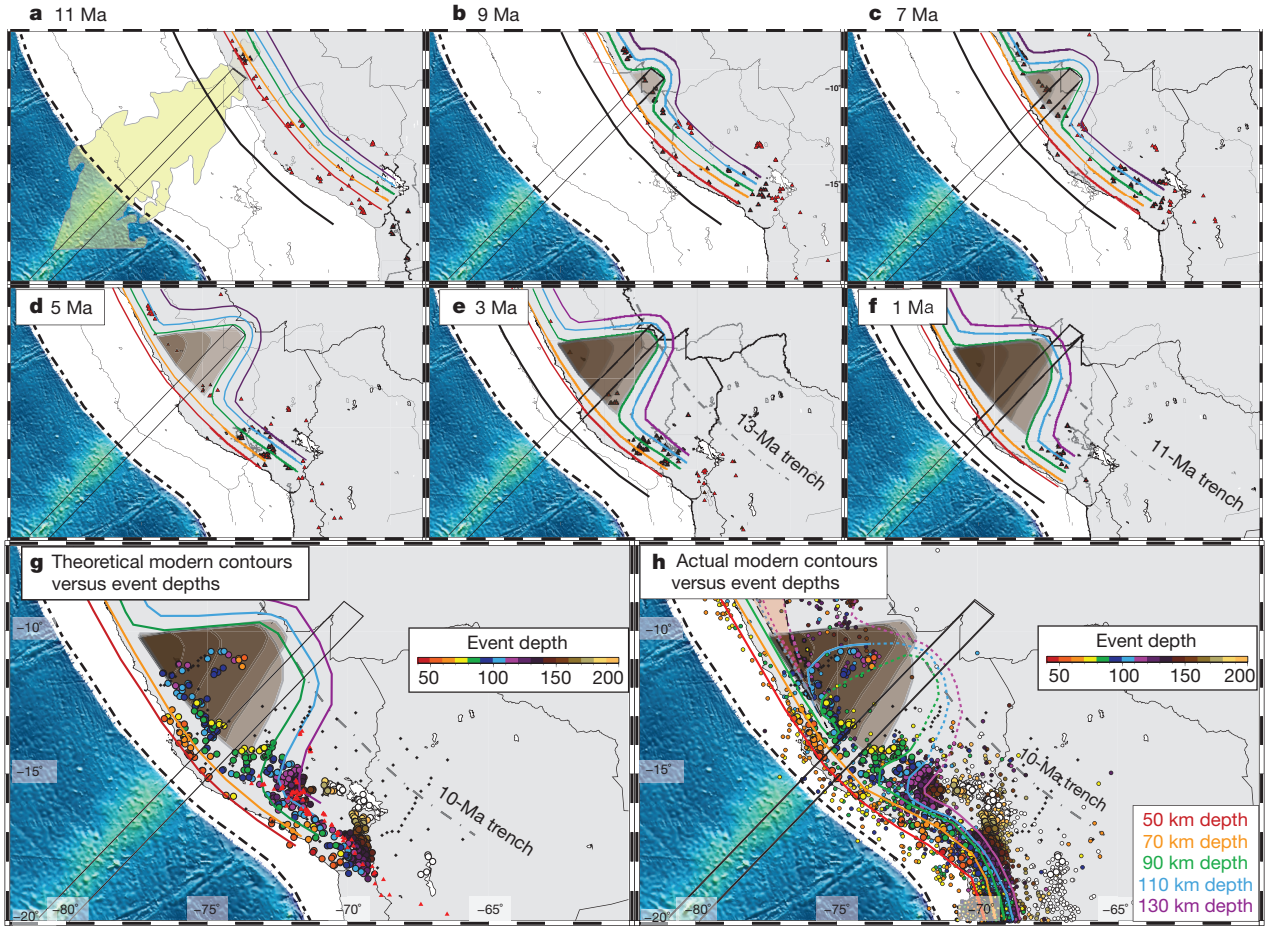

Figure 3 | Proposed evolution of the Peruvian flat slab. **a**–**f**, Proposed contours of the subducted slab, assuming that the ridge remains buoyant for 10 Ma after entering the trench. The approximate location of the subducted ridge is denoted by the black rectangular outline. Brown areas show areas of the continent underlain by flat slab at each time step. Triangles indicate volcanoes active during the 2 Myr following the time of the frame shown[22]. The location of the South American continent relative to the Nazca Ridge follows ref. 8. In **a**, we show the location of the projection of the mirror image of the Nazca Ridge (in yellow) that formed synchronously with the Nazca Ridge on the Pacific Plate when these plates were first created at the spreading centre following ref. 8. In **e**, red triangles show volcanism from 3 Ma to 2 Ma, and brown triangles show volcanism from 2 Ma to 1 Ma. In **f**, volcanism is shown for 1 Ma to 0 Ma (not including Holocene volcanism). **g**, Modern seismicity from this study (large circles) with depths >50 km, and contours as they would be if the removal of the ridge did not affect the longevity of the flat slab. **h**, Modern seismicity from this study and local seismicity at depth >50 km, as reported in the ISC catalogue for years 2004–2014, shown as smaller circles[17]. We plot our observed slab contours on the basis of our earthquake locations and the location of high-velocity anomalies in our tomographic results. Dashed lines indicate contours that are less certain, either because of a paucity of earthquakes or because they lie outside of our region of good tomographic resolution. The pink triangular shape shows the region with very limited seismicity that may indicate a slab window caused by tearing and the reinitiation of normal subduction.

some portion of the Nazca Ridge has resumed normal subduction. We propose that, over time, the kinetically slow conversion of basalt and gabbro to eclogite in the overthickened crust of the Nazca Ridge results in an increase in the density of the horizontal plate. Given the inboard extent of the modern flat slab, we propose that, approximately 10 Ma after entering the trench, the overthickened oceanic crust of the Nazca Ridge becomes sufficiently eclogitized that it is no longer neutrally buoyant and therefore resumes its vertical descent (Figs 2b, g and 3e–g).

Finally, modelling studies indicate that suction between the horizontal plate and overriding continental lithosphere hinders the removal of the flat slab[5]. In our study area, this is important because the portion of the continent under which the flat slab initially forms moves northwest relative to the ridge over time. To test whether the flat slab will perpetuate beneath these continental regions after the departure of the ridge, we apply the fourth principle to our model: continental regions previously underlain by the flat slab will continue to have flat slab beneath them for some time (brown regions in Fig. 3). This results in a broadening of the flat slab as new continental areas to the south become underlain by the ridge and associated flat slab, while areas to the north that were previously underlain by the ridge maintain their flat-slab geometry. This is consistent with earlier studies that attribute the along-strike (trench parallel) extent of the Peruvian flat slab to the southward sweep of the Nazca Ridge over time[8,9].

The proposed temporal evolution of the Peruvian flat slab shown in Fig. 3 combines the influences of trench retreat/overriding plate motion, suction, and ridge buoyancy. It assumes that the combination of all three forces is necessary for the formation of the flat slab, but that the first two are sufficient to perpetuate the flat slab after the departure of the ridge. A comparison between our conceptual model's slab geometry at present (Fig. 3g) with actual (observed) slab geometry (Fig. 3h) allows us to test these assumptions. The abrupt edge of the flat slab that we observe south of the ridge is very similar to that proposed by our conceptual model. We note that the dominant principle controlling the geometry of the flat slab here is the effect of ridge buoyancy, as there is no difference in trench rollback or continental lithospheric structure that might affect suction along strike in this region. Our observations therefore support the necessary contribution of the ridge to the formation of flat slabs, but are

also not inconsistent with additional contributions from suction and trench rollback.

Differences between the observed slab geometry and the geometry derived from our conceptual model are visible to the north of the ridge. In this area, the effect of the ridge is no longer present, and the geometry of the flat slab in our conceptual model is controlled by the effects of suction and trench rollback alone. Although both our conceptual model and our observations indicate a flat slab that broadens to the northwest of the ridge, the detailed morphologies are very different. In addition to an overall deepening of the flat slab north of the ridge (Fig. 3g, h and Extended Data Fig. 1), we observe a clear trench-parallel break in the subducted plate and a resumption of normal subduction trenchward of this tear (Figs 2a–c and 3h). This strongly suggests that, despite the presence of suction and trench rollback, the flat slab is no longer stable once the buoyant Nazca Ridge has been removed. Furthermore, once a break is present, the newly subducted plate assumes a normal steep dip angle, rather than a flat-slab geometry. In this study we are not able to resolve the northern extent of the Peruvian flat slab, nor can we establish the along-strike extent of the tear. However, International Seismological Centre Catalog locations north of our study area show a gap in seismicity that may be consistent with the absence of a flat slab because of a progressively tearing plate (Fig. 3h)[17]. The northward extent of the flat slab east of the tear may be due in part to the subduction of the Inca Plateau[8], although this is beyond the scope of our study.

Our model is applicable to all flat-slab geometries in cases for which a distinct change of dip angle is observed. This change in dip occurs at the depth at which the slab becomes neutrally buoyant. Our results may not be applicable to slabs when the dip angle is constant but very shallow[7] (for example, in Alaska and in the Cascadia region of the USA). Slabs that dip at a shallow angle sink at a constant rate, which is inconsistent with a period of neutral buoyancy. Such slabs may have effects that are similar to those produced by flat slabs, although they do not result in a complete cessation of arc volcanism (as occurred during the Laramide orogeny and is observed in Peru today), only its inboard deflection.

Our results may provide insights into the final stages of flat-slab subduction. Previous studies used volcanic patterns to reconstruct the formation and foundering of the Farallon flat slab in the western USA[2,18,19]. The diversity of models for the progression of this foundering is indicative of the insufficiency of the constraints provided by volcanic trends alone. Our results suggest that once the flat slab extends some distance away from the buoyant feature, it will begin to sink and/or tear. Tearing of the Farallon plate caused by an excessively wide flat slab may be consistent with tomographic images of broken fragments of the Farallon plate[20].

We conclude that flat slabs form through a combination of trench retreat, suction, and the inability of overthickened oceanic crust to sink below some depth (about 90 km) until sufficiently eclogitized to become negatively buoyant once again. Flat slabs that extend laterally beyond some critical distance from the buoyant overthickened crust will begin to founder, even in the presence of other factors such as suction and trench retreat. The Peruvian flat slab provides insights into the temporal evolution of flat slabs from initial shallowing to collapse, yielding new constraints for the reconstruction of flat-slab genesis and the nature of the flat-slab foundering.

Online Content Methods, along with any additional Extended Data display items and Source Data, are available in the online version of the paper; references unique to these sections appear only in the online paper.

Received 24 October 2014; accepted 28 May 2015.

1. Bedle, H. & van der Lee, S. Fossil flat-slab subduction beneath the Illinois basin, USA. *Tectonophysics* **424,** 53–68 (2006).
2. Humphreys, E. *et al.* How Laramide-age hydration of North American lithosphere by the Farallon slab controlled subsequent activity in the western United States. *Int. Geol. Rev.* **45,** 575–595 (2003).
3. Vogt, P. R. Subduction and aseismic ridges. *Nature* **241,** 189–191 (1973).
4. van Hunen, J., Van Den Berg, A. P. & Vlaar, N. J. On the role of subducting oceanic plateaus in the development of shallow flat subduction. *Tectonophysics* **352,** 317–333 (2002).
5. Manea, V. C., Pérez-Gussinyé, M. & Manea, M. Chilean flat slab subduction controlled by overriding plate thickness and trench rollback. *Geology* **40,** 35–38 (2012).
6. Gerya, T. V., Fossati, D., Cantieni, C. & Seward, D. Dynamic effects of aseismic ridge subduction: numerical modelling. *Eur. J. Mineral.* **21,** 649–661 (2009).
7. Skinner, S. M. & Clayton, R. W. The lack of correlation between flat slabs and bathymetric impactors in South America. *Earth Planet. Sci. Lett.* **371–372,** 1–5 (2013).
8. Rosenbaum, G. *et al.* Subduction of the Nazca Ridge and the Inca Plateau: insights into the formation of ore deposits in Peru. *Earth Planet. Sci. Lett.* **239,** 18–32 (2005).
9. Eakin, C. M. *et al.* Response of the mantle to flat slab evolution: insights from local S splitting beneath Peru. *J. Geophys. Res.* **41,** 3438–3446 (2014).
10. Ward, K. M. *et al.* Ambient noise tomography across the Central Andes. *Geophys. J. Int.* **194,** 1559–1573 (2013).
11. Phillips, K. & Clayton, R. W. Structure of the subduction transition region from seismic array data in southern Peru. *Geophys. J. Int.* **196,** 1889–1905 (2014).
12. Cahill, T., & Isacks, B. L. Seismicity and shape of the subducted Nazca plate. *J. Geophys. Res.* **97,** 17503–17529 (1992).
13. Hayes, G. P., Wald, D. J., & Johnson, R. L. Slab 1.0: a three-dimensional model of global subduction zone geometries. *J. Geophys. Res.* **117,** B01302 (2012).
14. Hasegawa, A., & Sacks, I. S. Subduction of the Nazca plate beneath Peru as determined from seismic observations. *J. Geophys. Res.* **6,** 4971–4980 (1981).
15. Uyeda, S., Watanabe, T., Ozasayama, Y. & Ibaragi, K. Report of heat flow measurements in Peru and Ecuador. *Bull. Earthquake Res. Inst.* **55,** 55–74 (1980).
16. Arrial, P. A. & Billen, M. I. Influence of geometry and eclogitization on oceanic plateau subduction. *Earth Planet. Sci. Lett.* **363,** 34–43 (2013).
17. International Seismological Centre. *On-line Bulletin* (ISC, http://www.isc.ac.uk (2012).
18. Liu, L. *et al.* The role of oceanic plateau subduction in the Laramide orogeny. *Nature Geosci.* **3,** 353–357 (2010).
19. Jones, C. H., Farmer, G. L., Sageman, B. & Zhong, S. Hydrodynamic mechanism for the Laramide orogeny. *Geosphere* **7,** 183–201 (2011).
20. Sigloch, K., McQuarrie, N. & Nolet, G. Two-stage subduction history under North America inferred from multiple-frequency tomography. *Nature Geosci.* **1,** 458–462 (2008).
21. Gripp, A. E. & Gordon, R. G. Young tracks of hotspots and current plate velocities. *Geophys. J. Int.* **150,** 321–361 (2002).
22. Instituto Geológico Minero y Metalúrgico. On-line catalog. (INGEMMET, http://www.ingemmet.gob.pe (2014).

Supplementary Information is available in the online version of the paper.

Acknowledgements We thank R. Clayton and P. Davies for providing the records from eight PERUSE stations. The PULSE experiment was supported by NSF grants EAR-0944184 (to L.S.W.), EAR-0943991 (to S.L.B.) and EAR-0943962 (to M.D.L.). The CAUGHT project was supported by NSF grants EAR-0908777 (to L.S.W.) and EAR-0907880 (to S.L.B.).

Author Contributions S.K.A. generated the tomographic model. L.S.W. developed the model of temporal evolution. A.K. provided earthquake locations. S.K.A, L.S.W. and A.K. developed the ideas and wrote the paper. S.L.B., M.D.L., G.Z., H.T. and C.C. contributed to data collection and paper editing.

Author Information Reprints and permissions information is available at www.nature.com/reprints. The authors declare no competing financial interests. Readers are welcome to comment on the online version of the paper. Correspondence and requests for materials should be addressed to S.K.A. (sknezevi@live.unc.edu).

METHODS

Earthquake locations. We use ANTELOPE software to auto-detect earthquakes, using a short-term average (STA) versus long-term average (LTA) trigger mechanism. The lengths of the STA and LTA moving time windows were chosen to be 1 s and 10 s respectively. After manually inspecting the waveforms, we selected 977 earthquakes out of 3,000 auto-detected events. We picked primary (P) and secondary (S, shear) wave arrival times for 673 slab events using SEISAN[23]. The selected events have the following characteristics: all events are in the depth range 50–310 km; travel-time misfit is less than 1 s; data are well recorded at a minimum of ten stations with azimuthal gap $\leq 270^\circ$ (see Supplementary Information).

For relative locations we use the program HYPODD[24] (Extended Data Fig. 1). We calculate differential times between P and S phases recorded at a common station for each event pair separated by ≤ 40 km. This interevent distance was interactively chosen after optimizing the linkage between the events in the first-step processing of phase data in HYPODD. Each event is strongly linked to a maximum of ten neighbouring events, having at least eight travel-time observations. We used the P-wave velocity model of ref. 25 for our starting model, and set the crustal thickness to 65 km. We used a V_p/V_s ratio of 1.75 to calculate S-wave velocities (where V_p is the P-wave velocity and V_s is the S-wave velocity).

Three-dimensional shear-wave imaging. The three-dimensional imaging of shear-wave velocity structure using earthquake-generated Rayleigh waves proceeds in two steps: first, we invert for Rayleigh wave phase velocities; subsequently, we invert the obtained phase velocities for shear-wave velocities. We use the two-plane wave method[26] to invert for Rayleigh wave phase velocities. Observations are modelled as a sum of two interfering plane waves, each described by its amplitude, phase and backazimuth. Predicted phase and amplitude values are calculated using finite frequency sensitivity kernels[27] that incorporate the (Born) single scattering approximation[28]. Amplitudes are corrected for geometrical spreading and attenuation. We examined 12 periods in the band between 0.007 Hz and 0.03 Hz, sensitive to V_s structure from the lower crust (~40-km depth), to the upper mantle (~200-km depth).

Data were collected from several seismic networks: PULSE[9], CAUGHT[10], PERUSE[11], and the global network permanent station in Lima, Peru. We picked fundamental mode Rayleigh waves for 65 well recorded teleseismic events (Extended Data Fig. 2a) with magnitudes ≥ 5.5.

We defined the study area with corners at 10° S, 69° W; 18° S, 79° W; 10° S, 69° W; and 10° S, 69° W (Extended Data Fig. 2b). The starting velocity model (Extended Data Fig. 2c) accounts for different crustal thicknesses across the study area[29]. We combine the IASPEI91 velocity model for the mantle[30] and the model of ref. 31 for the crust and use a forward algorithm[32] to predict phase velocities across the study region.

The inversion is regularized with model covariances set to 0.15 km s^{-1}. The choice of regularization parameter is based on the stability of both Rayleigh-wave and shear-wave inversions. Longer periods are generally less well resolved than shorter periods because of their broader sensitivity kernels. The best resolved areas are beneath the Western Cordillera, Altiplano, Eastern Cordillera, and coastal forearc and, to a lesser extent, the Sub-Andean zone (Extended Data Fig. 3a). The resolution within the foreland basin is mostly confined along the stations deployed in foreland basin in eastern Peru.

In the second step, we invert obtained phase velocities (Extended Data Fig. 4) for one-dimensional shear-wave velocities[32,33]. We use the same starting model as in the previous step (Extended Data Fig. 2c). Sensitivity kernels for longer periods are substantially broader than the sensitivity kernels for shorter periods, and sample greater depths. The peak sensitivities for the periods used in this study range from depths of ~40 km (for 33 s) up to ~200 km (for 143 s). Thus, the vertical resolution is greatest between ~40 km and ~200 km, and decreases gradually with depth (below ~300 km, resolution drops below 0.1; Extended Data Fig. 3b). The model covariance obtained for phase velocities from the two-plane wave method was used as data covariance to regularize the shear wave velocity inversion. The average root mean squared (r.m.s.) misfit between predicted and observed phase velocities over all periods indicates an average error of ~0.02 km s^{-1} (Extended Data Fig. 3c). Results of our shear-wave inversions are presented in Fig. 2 and Extended Data Fig. 5.

Lateral and vertical resolution. The main new features observed in this study from the surface-wave tomography include the far inboard extent of flat slab along the subducting Nazca ridge, and the slab tear north of the ridge. We performed a range of tests to investigate lateral and vertical resolution to ensure the robustness of these features (see also Extended Data Figs 3, 6–10).

Lateral resolution. We plot the resolution matrix rows of isolated model parameters for several periods, with an emphasis on the spatial resolution at three locations along the northern profile north of the subducting Nazca Ridge: one where we observe re-steepening of the slab, one at the slab tear, and one along the flat-slab remnant. We also investigate points at two locations along the subducting Nazca Ridge: one where we observe the far inboard extent of the flat slab ('long flat slab'), and one where previous studies[12] suggest the end of flat slab should be ('short flat slab'). The examination of our resolution matrix for these five selected nodes is intended primarily to demonstrate that we have sufficient spatial resolution to resolve the slab tear north of the ridge and the inboard extent of flat slab along the ridge. We focus on intermediate periods because they have peak sensitivity at the most relevant depths (Extended Data Fig. 2c). The tests show that these model parameters are able to resolve spatial-scale features smaller than those discussed here. The only node for which we observe a particularly broad sensitivity cone is the one at the far inboard extent of the flat slab. This finding suggests that, while the inboard extent of the flat slab may not be as well resolved as in other locations, a shorter flat slab would have been imaged accurately if it did exist. Our inboard extent is therefore a conservative estimate.

To demonstrate the sensitivity of our results to grid node spacing, we plot phase-velocity maps for intermediate periods using 0.25° and 0.5° grid node spacing. The phase velocity maps with 0.5° grid node spacing show major features that are smoother than, but consistent with, major features that are observed on maps with 0.25° spacing. Further, the dispersion curves for the five selected nodes reflect consistency regardless of the grid node spacing. Along the northern profile in both cases we observe faster anomalies at 66 s and 77 s, where we observe the re-steepened slab, slow anomalies at all intermediate periods where we observe the slab tear, and fast anomalies where we observe the flat-slab remnant. Along the flat-slab profile we note low phase velocities at the location where previous studies suggest a resumption of the steep slab, and high phase velocities at the location which we propose to be the end of flat slab.

We perform a series of checkerboard tests using the surface wave resolution matrices to test the size of the anomalies that can be recovered with the varying periods used here (Extended Data Fig. 6). These tests show whether we have sufficient spatial resolution to recover the size of the anomaly analogous to the observed tear and whether we have sufficient resolution to resolve the inboard extent of the flat slab. For this reason we plot the five selected nodes. In addition, these tests yield a better understanding of the spatial resolution of phase velocity maps across the study area and easily reveal areas that suffer from smearing (because of preferential ray path direction and/or lack of data). Short and intermediate periods, with peak sensitivities between 50-km and 150-km depth, are able to recover smaller anomalies, equal to and smaller than the lateral extent of the observed slab tear. The tests show that we do have sufficient spatial resolution to resolve the slab tear, flat slab remnant to the east, and re-steepened slab to the west. Longer periods, which mostly sample subslab material, can recover slightly larger features. However, both shorter and longer periods are able to resolve the size of the anomaly analogous to subducting slab at the end of the flat slab. These checkerboard tests show that we are able to resolve anomalies where previous studies suggested the end of flat slab, while the node representing the far inboard extent of flat slab may be streaked because of a lack of crossing rays. Thus, on the basis of these tests, we can conclude with confidence that the inboard extent of flat slab along the subducting Nazca Ridge is not where previously assumed, but further inboard. Resolution at the location representing the far inboard extent of flat slab is weak and suffers from smearing. However, our conclusion on the far inboard extent of flat slab is supported by constraints from other studies[34,35].

Vertical resolution. We test our vertical resolution along all profiles shown in Fig. 2. Extended Data Figures 7–10 show recovery tests for: the southern profile, where we observe steeply dipping slab (Extended Data Fig. 7); the flat-slab segment along the Nazca Ridge (Extended Data Fig. 8); just north of the Nazca Ridge, where we observe deepening of earthquakes and the start of slab tear (Extended Data Fig. 9); and the northern profile, where we observe the slab tear, re-steepening of the slab and flat-slab remnant (Extended Data Fig. 10).

Extended Data Fig. 7 demonstrates our ability to recover a dipping slab south of the ridge. We model a shear wave velocity structure with a 70-km-thick steeply dipping slab associated with a velocity of 4.6 km s^{-1} (Extended Data Fig. 7d). This model is based on our interpretations of the observed structures that we show in Fig. 2d. We predict dispersion curves for this model using the code of ref. 32, add noise to predicted phase velocities, and invert them using the same starting model (Extended Data Fig. 7b) and regularization parameters as for the model shown in Extended Data Fig. 7c. The Gaussian noise was generated from misfits obtained in our final model using the central limit theorem method, and randomly assigned to predicted phase velocities. We were able to recover the steeply dipping structure, but its thickness appears greater owing to vertical smearing. We were not able to recover the full amplitude of the anomaly, but a somewhat lower amplitude (4.45–4.55 km s^{-1}). Our model calculated using observed data (Extended Data Fig. 7c) indicates shear-wave velocities above 4.55 km s^{-1}. This recovery test suggests that, in order to fully recover the amplitude of observed high shear-wave velocities, either the slab in Extended Data Fig. 7d needs to be associated with velocities greater than 4.6 km s^{-1}, or the thickness of the slab should be greater, or both.

Extended Data Figure 8 demonstrates our ability to differentiate between a flat slab with our (greater) inboard extent along the Nazca ridge track ('long flat slab') and a flat slab with shorter extent, suggested previously[12] (Extended Data Fig. 8g, 'short flat slab'). The plots in Extended Data Fig. 8h and i show recovered models. The tests show that we are able to recover the flat-slab-related high shear-wave velocities. However, we observe vertical smearing, and notice that, in the recovered model, slab-related high velocities appear at shallower depths, resulting in high velocities in the lower crust and more shallow flat slab. This is also noticeable in our model shown in Extended Data Fig. 8e. Owing to vertical smearing and the gradational nature of the slab–mantle boundary in oceanic plates, the bottom of the slab is poorly resolved. Different layer discretization owing to different crustal thicknesses causes the artificial undulating nature of the slab's positive anomaly, also present in our model (Extended Data Fig. 8e). The plots in Extended Data Fig. 8h, i demonstrate sufficient vertical resolution to recover the end of the flat slab. We also plot dispersion curves at two points, representing the shorter end of flat slab previously suggested[12] (Extended Data Fig. 8b) and the far inboard end (Extended Data Fig. 8c). Dispersion curves predicted for shorter and longer flat slab are substantially different and the observed phase velocities match better with the longer flat slab.

Extended Data Figure 9 demonstrates our ability to recover a torn slab to the north of the Nazca ridge. Extended Data Figure 10 demonstrates our ability to distinguish between torn slab and a continuous slab along the northernmost profile. Extended Data Figure 10i, j shows that lateral heterogeneities and dipping structures are well recovered (except at shallower depths, where we lose resolution; Extended Data Fig. 3b). Again, we are able to recover the flat slab, but with evident vertical smearing. The observed dispersion curves at locations at which we observe the re-steepened slab (point 1), torn slab (point 2) and flat-slab remnant (point 3) are very different. Shorter periods of the torn slab model at point 1 are characterized with low phase velocities, while intermediate periods have much higher phase velocities. In contrast, the continuous slab model is associated with high phase velocities at both short and intermediate periods. At point 2 both short and intermediate periods show low phase velocities for the torn slab model, but high phase velocities for the continuous slab model. At point 3 both short and intermediate periods are associated with high phase velocities for both torn and continuous flat slab. Generally, we are able to reproduce the observed dispersion curves with our model of torn slab (Fig. 2d), except for the low phase velocities at shorter periods at point 1. This is because we did not introduce low shear velocities in the lower crust in our starting model. Dispersion curves for the continuous flat slab differ from those observed at points 1 and 2, especially at intermediate periods that sample upper mantle material.

23. Lienert, R. B., Berg, E. & Frazer, L. N. HYPOCENTER: an earthquake location method using centered, scaled, and adaptively damped least squares. *Bull. Seismol. Soc. Am.* **76,** 771–783 (1986).
24. Waldhauser, F. & Ellsworth, W. L. A double-difference earthquake location algorithm: method and application to the Northern Hayward Fault, California. *Bull. Seismol. Soc. Am.* **90,** 1353–1368 (2000).
25. Dorbath, C. Velocity structure of the Andes of central Peru from locally recorded earthquakes. *J. Geophys. Res.* **23,** 205–208 (1996).
26. Forsyth, D. W. & Li, A. in *Seismic Earth: Array of Broadband Seismograms* (eds Levander, A. & Nolet, G.) 81–98 (Geophysical Monograph Series 157, 2005).
27. Yang, Y. & Forsyth, D. W. Regional tomographic inversion of the amplitude and phase of Rayleigh waves with 2-D sensitivity kernels. *Geophys. J. Int.* **166,** 1148–1160 (2006).
28. Zhou, Y., Dahlen, F. A. & Nolet, G. Three-dimensional sensitivity kernels for surface wave observables. *Geophys. J. Int.* **158,** 142–168 (2004).
29. Tassara, A., Götze, H.-J., Schmidt, S. & Hackney, R. Three-dimensional density model of the Nazca plate and the Andean continental margin. *J. Geophys. Res.* **111,** B09404 (2006).
30. Kennett, B. L. N. *IASPEI 1991 Seismological Tables* (Bibliotech, 1991).
31. James, D. E. Andean crustal and upper mantle structure. *J. Geophys. Res.* **76,** 3246–3271 (1971).
32. Saito, M. in *Seismological Algorithms: Computational Methods and Computer Programs*. (ed. Doornbos, D. J.) 293–319 (Elsevier, 1988).
33. Weeraratne, D. S., Forsyth, D. W., Fischer, K. M., & Nyblade, A. A. Evidence for an upper mantle plume beneath the Tanzanian craton from Rayleigh wave tomography. *J. Geophys. Res.* **108,** 2427 (2003).
34. Scire, A. *et al.* Imaging the transition from flat to normal subduction: variations in the structure of the Nazca slab and upper mantle under southern Peru and northwestern Bolivia. *Geophys. J. Int.* (submitted).
35. Snoke, J. A., Sacks, I. S. & Okada, H. Determination of the subducting lithosphere boundary by use of converted phases. *Bull. Seismol. Soc. Am.* **67,** 1051–1060 (1977).

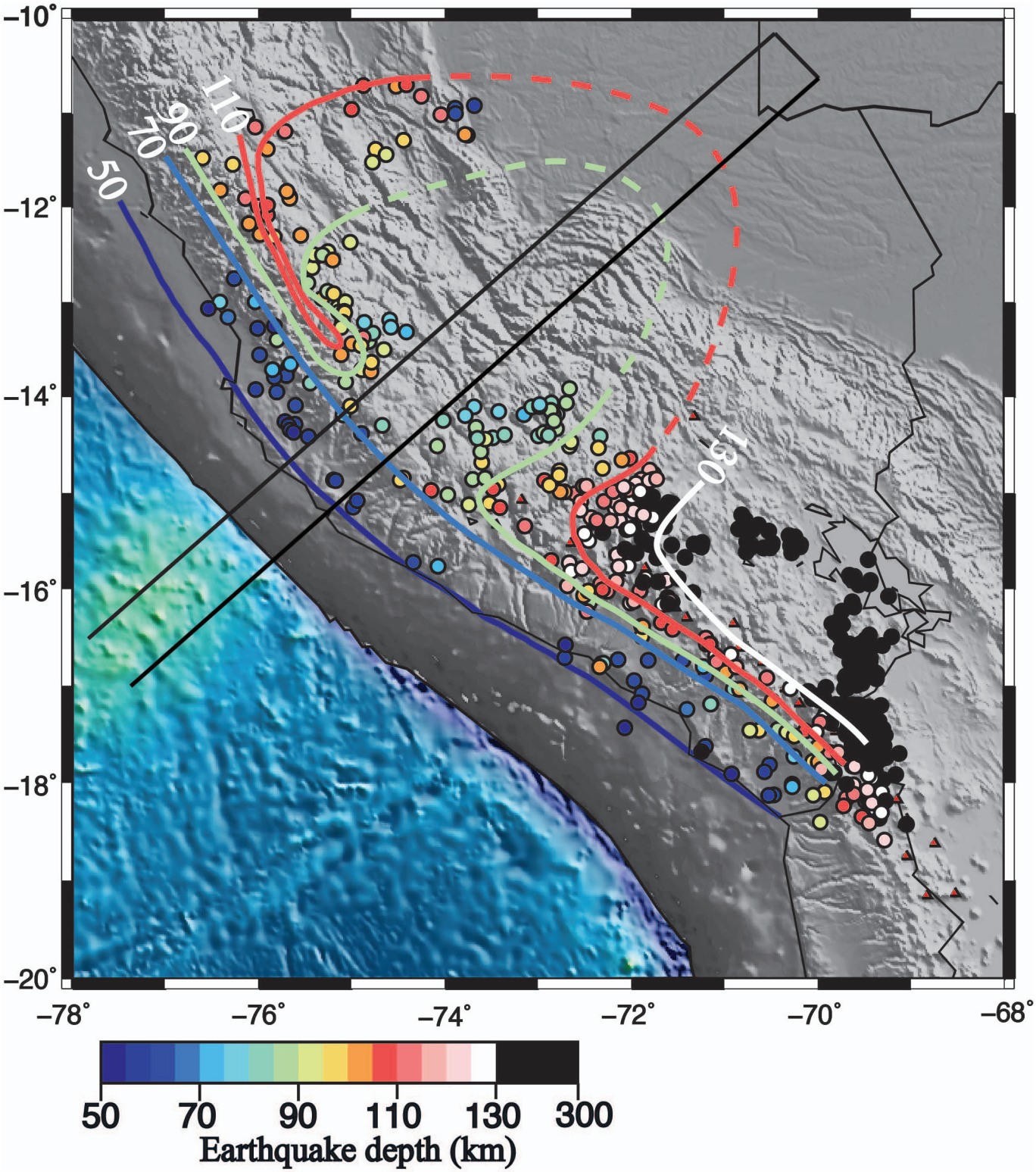

Extended Data Figure 1 | Relocated earthquakes used in this study. Colours show the depth of events (in km) and lines indicate the slab contours in 20-km depth increments. Events below 130 km are shown in black.

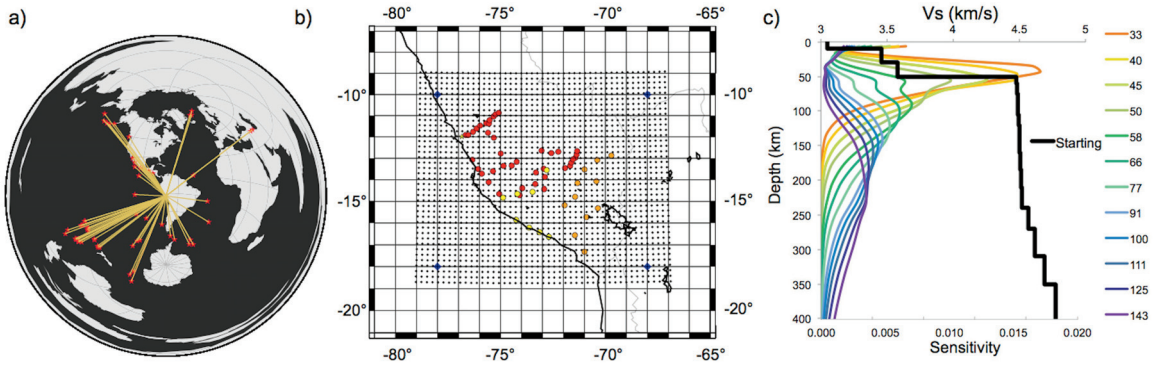

Extended Data Figure 2 | Events, grid and starting model used for the Rayleigh wave phase velocity inversions. **a**, Teleseismic events used in the study. **b**, Black diamonds represent grid nodes; blue diamonds represent corners used in the two-plane wave methodology; red circles are PULSE stations; orange circles are CAUGHT stations; yellow circles are PERUSE stations; and yellow star is the permanent NNA station. **c**, Sensitivity kernels for periods used in our study with the one-dimensional starting shear wave velocity model.

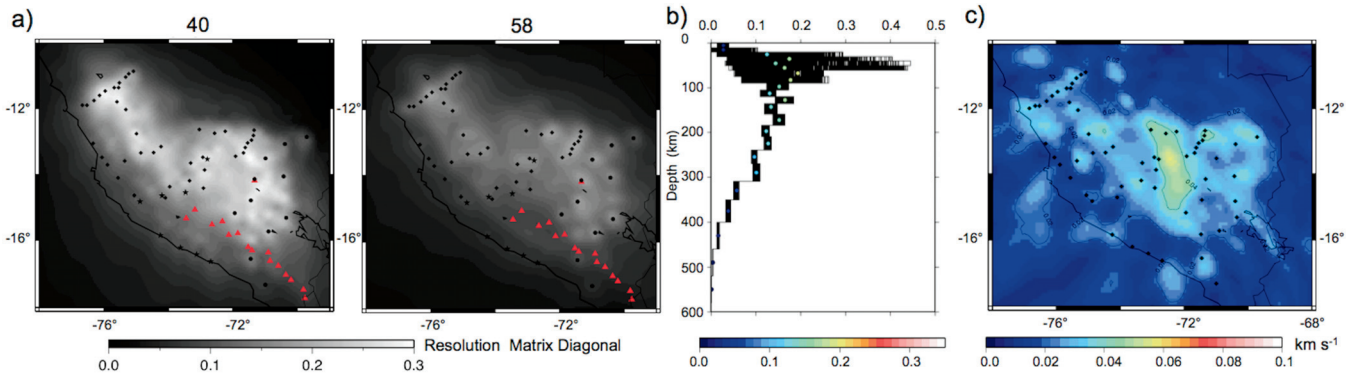

Extended Data Figure 3 | Lateral and vertical resolution. **a**, Resolution for the 40-s and 58-s periods. The resolution matrix diagonal for Rayleigh wave phase velocities is indicated in grey scale. Red triangles are Holocene volcanoes. Black rectangles, circles and stars are stations used here. **b**, Resolution matrix diagonal values for all one-dimensional shear wave velocity inversions. Colours of the circles indicate average values of the resolution matrix diagonals for each layer. **c**, The r.m.s. average misfit over all periods at each point after our shear wave inversions. Colours represent the misfit in km s^{-1}. Black rectangles represent stations used in our study.

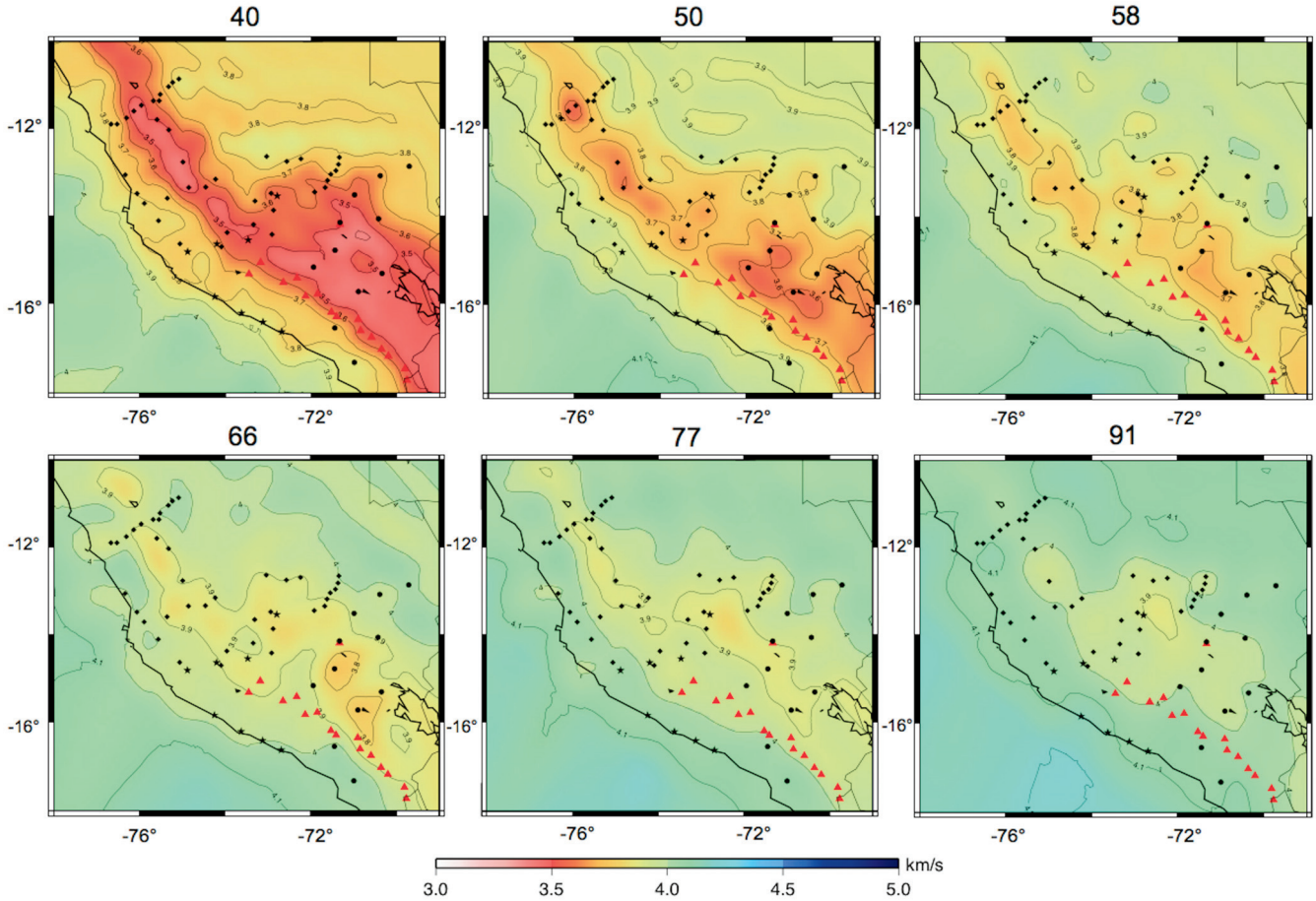

Extended Data Figure 4 | Calculated Rayleigh wave phase velocities for 40-s, 50-s, 58-s, 66-s, 77-s and 91-s periods. Colours and contours indicate absolute phase velocities. Red triangles represent Holocene volcanoes. Black rectangles, circles and stars represent stations used in our study.

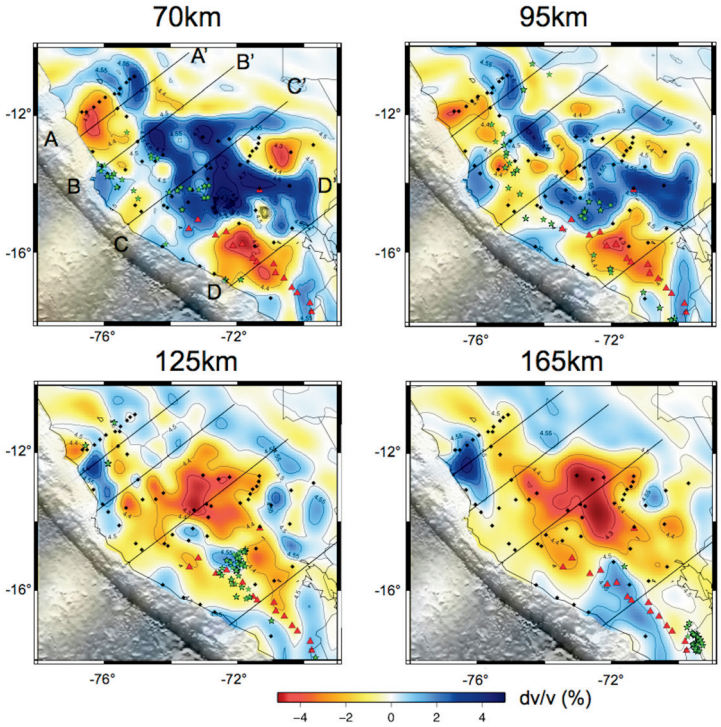

Extended Data Figure 5 | Shear wave velocity maps at depths of 70 km, 95 km, 125 km and 165 km. Colours represent velocity deviations with respect to the reference model (Extended Data Fig. 2c); contours show absolute velocities. Green stars indicate earthquakes within a depth of 20 km relocated using HypoDD[24]. Red triangles represent Holocene volcanoes. Black rectangles, circles and stars are stations used in our study.

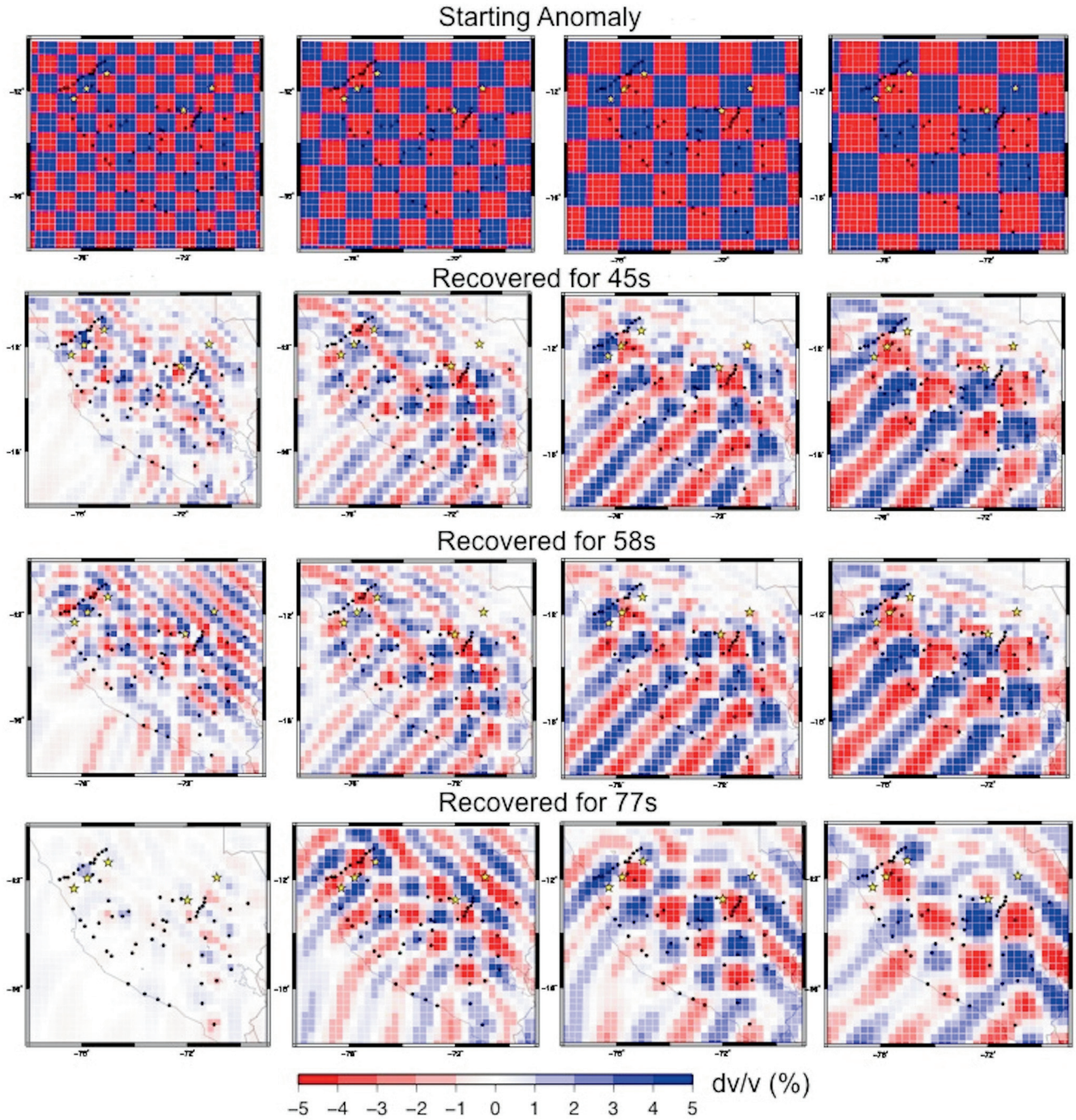

Extended Data Figure 6 | Checkerboard tests estimated from resolution matrix for 45 s, 58 s and 77 s. Colours represent the recovered anomaly. Yellow stars along the northernmost profile indicate locations where we observe re-steepening of the slab, slab tear and the flat-slab remnant; the two stars along the subducting Nazca Ridge refer to locations of our (greater) inboard extent along the Nazca ridge track and a flat slab with shorter extent suggested previously[12].

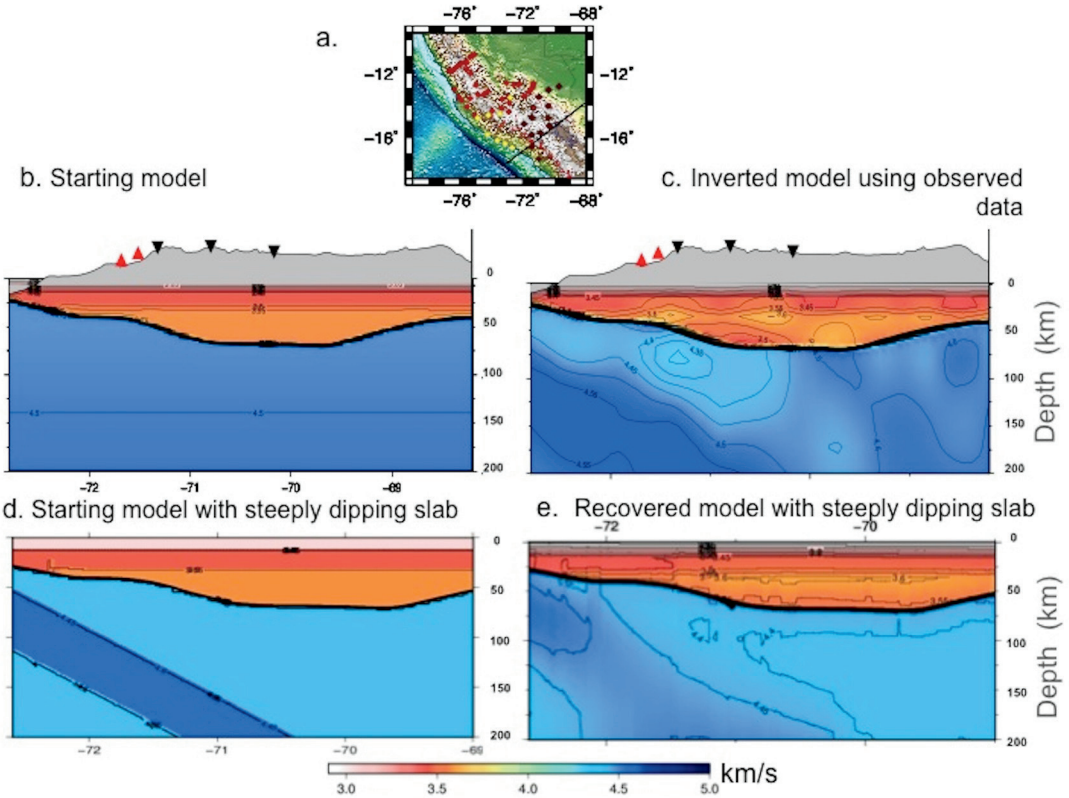

Extended Data Figure 7 | Recovery tests for the dipping slab south of the ridge. **a**, Map showing the transect and stations locations (rectangles). **b**, Starting model used in the shear wave velocity inversion; contour lines and colours are absolute shear-wave velocities; black inverted triangles are stations within 35 km of the transect; red triangles are Holocene volcanoes. **c**, Model calculated using observed data. **d**, Model based on our interpretations of the observed structures (see also Fig. 2d). **e**, Recovered model.

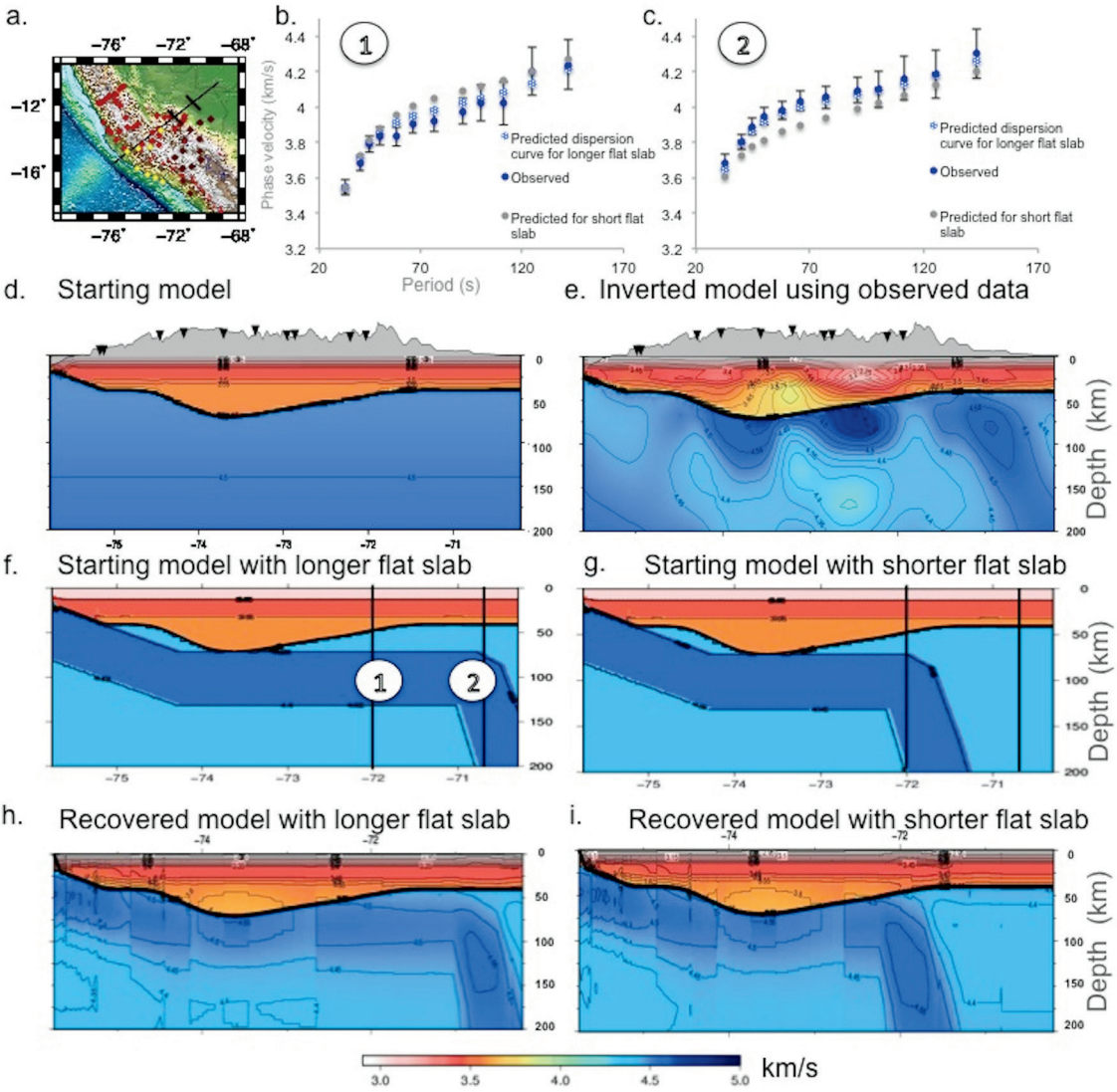

Extended Data Figure 8 | Recovery tests for the flat-slab segment. **a**, Transect. **b**, Dispersion curve at a location representing the shorter end of flat slab previously suggested[12]. **c**, Dispersion curve at a location representing the greater inboard extent of flat slab (proposed here); error bars represent one standard deviation of uncertainty. **d**, Starting model. **e**, Model calculated using observed data. **f**, Model with our (greater) inboard extent of flat slab. **g**, Model with shorter flat slab as suggested previously[12]. **h**, Recovered model from **f**. **i**, Recovered model from **g**.

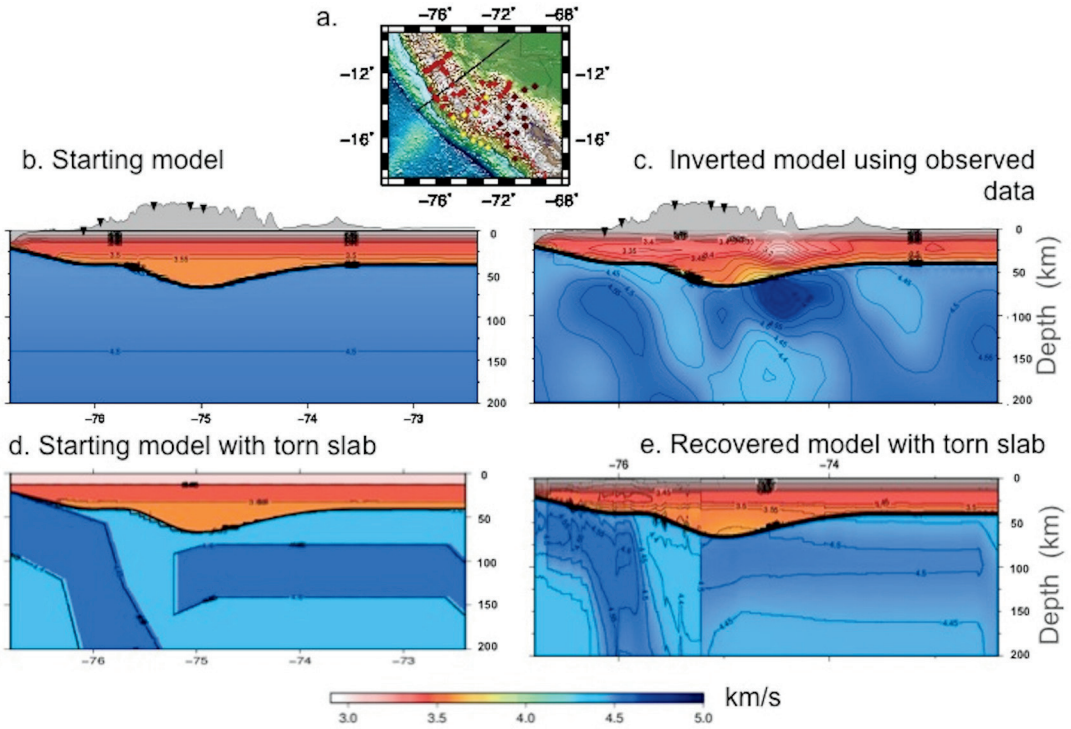

Extended Data Figure 9 | Recovery tests for the area just north of the Nazca Ridge, where we observe a deepening of earthquakes, and the southern end of the slab tear. **a**, Reference map. **b**, Starting model. **c**, Model calculated using observed data. **d**, Model based on our interpretations of the torn slab (see Fig. 2d). **e**, Recovered model.

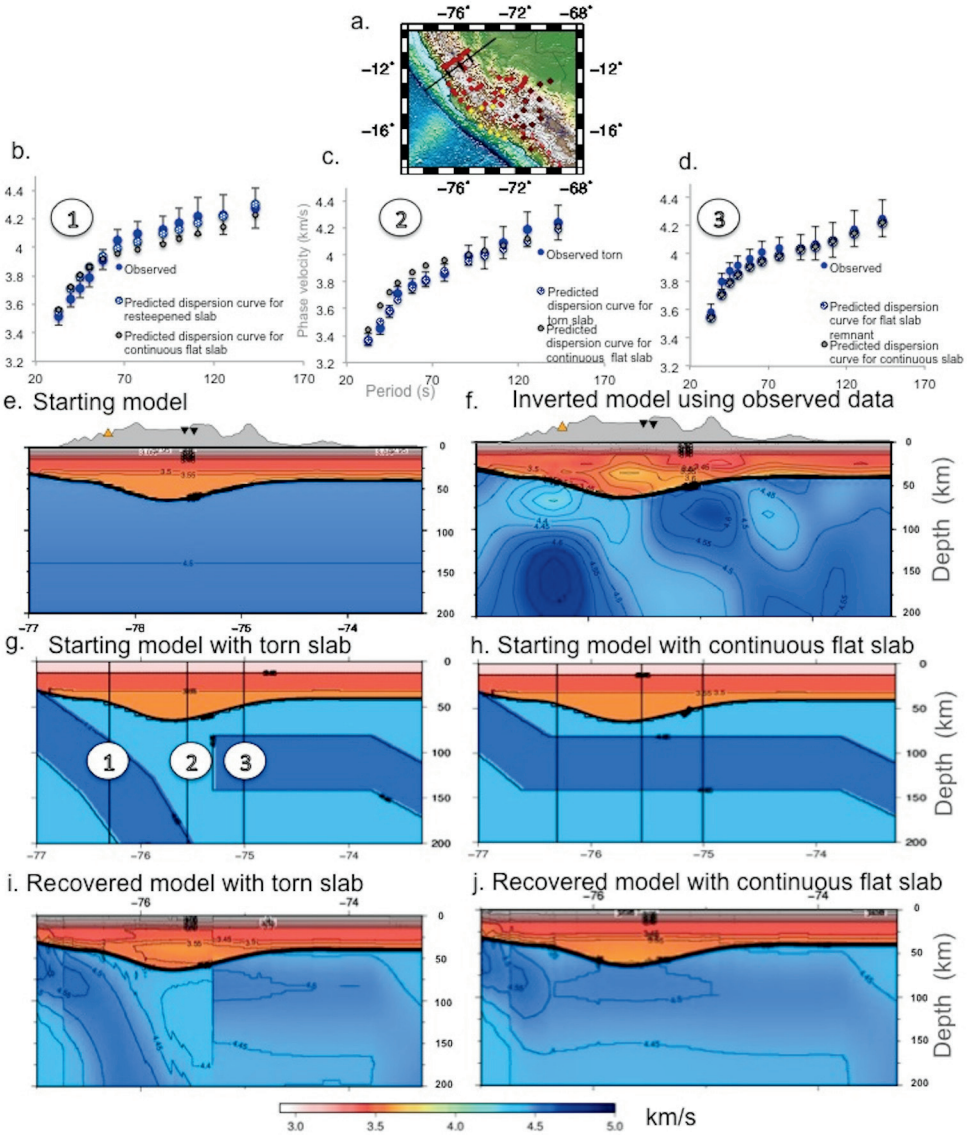

Extended Data Figure 10 | Recovery tests for the northern profile where we observe the slab tear, a re-steepening of the currently subducting slab west of the tear, and the flat slab remnant east of the tear. **a**, Transect. **b**, Dispersion curve at the location representing the re-steepened slab; error bars represent one standard deviation of uncertainty. **c**, Dispersion curve at location representing the slab tear. **d**, Dispersion curve at location representing the flat slab remnant. **e**, Starting model. **f**, Model calculated using observed data. **g**, Model with slab tear that we propose in this study. **h**, Model with continuous flat slab suggested previously suggested in ref. 12 and other studies. **i**, Recovered model from **g**. **j**, Recovered model from **h**. See Methods for further explanation.